

www.acsami.org Research Article

# Tuning Site Energy by XO<sub>6</sub> Units in LiX<sub>2</sub>(PO<sub>4</sub>)<sub>3</sub> Enables High Li Ion Conductivity and Improved Stability

Zhiwei He, Bingkai Zhang,\* Jiajie Zhong, Zhan Lin,\* and Feng Pan\*



Cite This: ACS Appl. Mater. Interfaces 2021, 13, 50948-50956



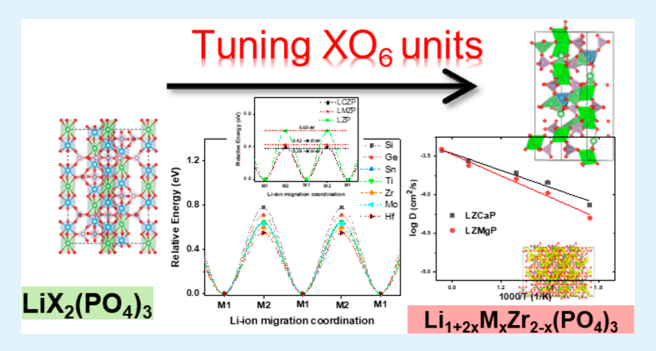
**ACCESS** 

Metrics & More

Article Recommendations

Supporting Information

**ABSTRACT:** Solid-state electrolytes (SSEs) with high ion conductivity are necessary for all-solid-sate lithium ion batteries. Here, a less studied NASICON-type  $\text{LiZr}_2(\text{PO}_4)_3$  (LZP) is screened out from seven LXP compounds ( $\text{LiX}_2(\text{PO}_4)_3$ , X = Si, Ge, Sn, Ti, Zr, Hf, and Mo), which combines the electrochemical stability with high Li conductivity. The bond valence site energy (BVSE), climbing image nudged elastic band (Cl-NEB) method, and electrochemical phase diagram prove LZP has a lower Li migration barrier and the largest electrochemical stability window. The underlying reason for high Li conductivity is analyzed from the structural features to the electronic structures. Furthermore, the XO<sub>6</sub> unit mixed frameworks  $\text{Li}_{1.667}\text{Ca}_{0.333}\text{Zr}_{1.667}(\text{PO}_4)_3$  (LCZP) and  $\text{Li}_{1.667}\text{Mg}_{0.333}\text{Zr}_{1.667}(\text{PO}_4)_3$ 



(LMZP) exhibit high Li ion conductivity associated with a very low Li migration barrier (~0.20 eV). This work opens a new avenue of broad compositional spaces in LXP for SSEs.

KEYWORDS: NASICON-type LXP, solid-state electrolyte, ionic conductivity, stability, first-principle calculations, all-solid-state lithium ion battery

## 1. INTRODUCTION

All-solid-state lithium batteries (ASSLBs) have recently been extensively studied due to their high lithium capacity and high safety. 1-4 Currently, the use of solid-state electrolytes (SSEs) with high ionic conductivity and electrochemical stability is a field of continuous interest in ASSLBs. 5,6 NASICON-type fast Li ion conductors are potential alternatives for SSEs, generally with a rhombohedral unit cell and space group  $R\overline{3}c$ , that is,  $LiX_2(PO_4)_3$  phosphates (LXP, X = Si, Ge, Ti, Sn, Zr, Hf, and Mo). 7,8 Among LXP, formula LiTi<sub>2</sub>(PO<sub>4</sub>)<sub>3</sub> (LTP) and Aldoped LATP (Li<sub>1.3</sub>Al<sub>0.3</sub>Ti<sub>1.7</sub>(PO<sub>4</sub>)<sub>3</sub>) have been extensively studied.<sup>9,10</sup> The bulk ionic conductivity for LATP at room temperature (298 K) is about 1.0 mS cm<sup>-1</sup> with low activation energy (0.25 eV). However, compared to the liquid electrolytes (LEs), the overall rate performance of LATP in a state-of-the-art ASSLBs setup is not satisfactory due to three main obstacles: (1) the reduction of Ti<sup>4+</sup> to Ti<sup>3+</sup>, (2) the formation of an MCI (mixed conducting interphase) at a Limetal anode, and (3) the inferior ionic conductivity to LEs. 12,13

The framework of LXP consists of three local structural units: PO<sub>4</sub> tetrahedra, XO<sub>6</sub> octahedra, and LiO<sub>6</sub> octahedra, which can be regarded as "material genes" and determine the Li ion diffusion and electrochemical stability. However, most development efforts are now focused on improved conductivity and stability in LTP and LATP, while neglecting the other LXP structures. Although tuning local non-lithium

structural units within this framework could affect Li ion conductivity and stability, there is a lack of systematic study about which LXP has the highest expectations to overcome the key challenge of combining stability with ultrafast lithium diffusivity. Moreover, the effects of divalent cation doping on Li ion conductivity and stability within LXP are also less investigated. <sup>16</sup>

In this study, our main focus is to adopt approaches correlating Li ion conductivity to find and design LXP SSEs with enhanced conductivity and stability, which will also be beneficial to understand Li ion transport mechanisms and properties. We employ the well-studied LXP framework and the concept of the Li ion cooperative migration mechanism to develop an insight into the influence of  $XO_6$  units. We find the  $\text{LiZr}_2(PO_4)_3$  (LZP) with  $\text{ZrO}_6$  units has a potential for high Li ion conductivity and good electrochemical stability because of the structural (large size of Li ion migration channel) and electronic (weak interaction of Zr-O bond and low energy level of  $(\text{Zr-O})^*$  antibonding orbitals) properties. Moreover, there is an improved ionic conductivity upon Ca and Mg

Received: August 2, 2021 Accepted: October 8, 2021 Published: October 23, 2021





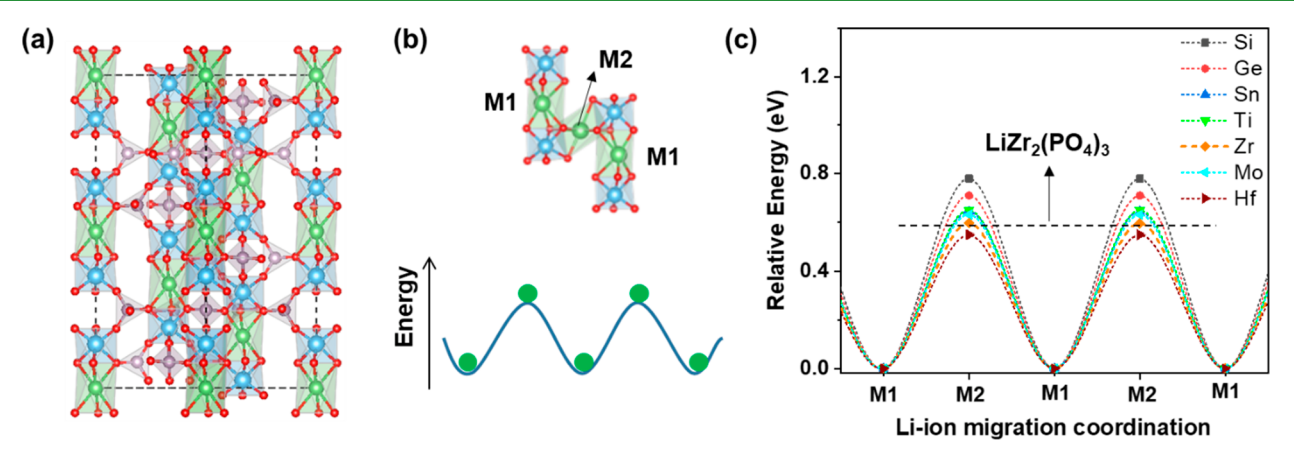


Figure 1. (a) Side view of LiX(PO<sub>4</sub>)<sub>3</sub> crystal structure. (b) Local configuration with two Li sites (M1 and M2) and XO<sub>6</sub> octahedral units along the Li ion migration channel. The lower inset is the energy profile along the Li ion migration channel shaped by M1 and M2 sites. (c) Relative energies at M1 and M2 sites along Li ion migration channels within different LXP structures. The light green and cyan polyhedrons represent LiO<sub>6</sub> and XO<sub>6</sub> units, respectively. The red, cyan, green, and pink spheres represent O, X, Li, and P atoms, respectively.

incorporation in the LZP framework due to the distorted LiO<sub>x</sub> polyhedrons. Finally, we summarize that tuning XO<sub>6</sub> structural units in a NASICON-type framework improves Li ion conductivity with good electrochemical stability, which would enable the engineering and search for next-generation

## 2. COMPUTATIONAL DETAILS AND STRUCTURAL **MODELS**

The density functional theory (DFT)-based first-principle calculations are performed in the software of the Vienna ab initio simulation package (VASP).<sup>17</sup> The Kohn-Sham orbitals for the valence electrons are expanded with the projector augmented wave (PAW) approach. 18 The generalized gradient approximation (GGA) level DFT functional, PBE, is employed to describe the exchange-correlation function. 19,20 The Monkhorst-Pack method is performed to sample the Brillouin zone (BZ). The cutoff energy is 500 eV, and the BZ is sampled with  $3 \times 3 \times 2$ . All atomic positions are optimized until the residual force is <0.01 eV/Å, and the optimization of the LXP cell continues until the change in total energy is  $<1.0 \times 10^{-4}$ 

To study the effect of XO<sub>6</sub> units on the potential energy surface of Li ion, we calculate the relative site energy of Li ions in LXP  $E_{\text{site-energy}}$ , which is defined as

$$E_{\text{site-energy}}(\text{LXP}) = E_{\text{M2-site}}(\text{LXP}) - E_{\text{M1-site}}(\text{LXP})$$
 (1)

where  $E_{\text{M1-site}}(\text{LXP})$  and  $E_{\text{M2-site}}(\text{LXP})$  represent all Li ions residing at M1 sites in LXP and migrating one Li ion from the M1 site to M2 sites in LXP, respectively. To evaluate the bond strength of the Li-O bond in LXP, the Li binding energy is calculated by the equation

$$E_{\rm binding\text{-}energy}(\text{Li-O}) = E_{\rm LXP\text{-}Li\_vacancy} + E_{\rm Li\_metal} - E_{\rm LXP} \end{center}$$

where  $E_{\rm LXP-Li\_vacancy}$ ,  $E_{\rm Li\_metal}$ , and  $E_{\rm LXP}$  are the energy of bulk LXP with one Li vacancy, Li metal, and the bulk LXP, respectively. The vacancy migration barrier in LXP is performed by using the Cl-NEB method.<sup>21</sup> The Li ion diffusion coefficient (D) in the LXP systems is obtained by using ab initio molecular dynamics (AIMD) simulations with a Gamma-only k-point and NVE ensemble.  $^{22}$  The time step and the total simulation time for AIMD are 2 fs and 230 ps,

respectively. The diffusion coefficient D is defined in terms of the mean-square displacement (MSD) over time. For more information about AIMD, see the Supporting Information.

The electrochemical stability window of LXP is the applied voltage (V vs Li+/Li) range between which LXP does not get oxidized or reduced. For  $\mu_{Li} = 0$  (0 V),  $\mu_{Li}$  is the lithium chemical potential. Calculations to construct electrochemical stability phase diagrams are performed within the database (Open Quantum Materials Database) consisting of DFTcomputed bulk energies of materials. The grand potential convex hulls at a given voltage are formed by the grand potentials of a set of compounds and their linear combinations that minimize the grand potential at each compound. Using these convex hulls at different voltages, we can evaluate the electrochemical stability window of LXP by using the Grand Canonical Linear Programming (GCLP) technique. 23,24 More information about the calculations of electrochemical stability is detailed in previous studies.<sup>25–29</sup>

## 3. RESULTS AND DISCUSSION

3.1. Enhancing Ionic Conductivity and Stability of LXP by Tuning XO<sub>6</sub> Units. The NASICON-type LXP crystal structure has hexagonal symmetry and is composed of facesharing XO<sub>6</sub>-LiO<sub>6</sub>-XO<sub>6</sub> units along the c-axis which are linked by PO<sub>4</sub> tetrahedrons (Figure 1a). There are two main Li sites (M1 and M2) in LXP, as shown in Figure 1b. Using firstprinciples calculation, previous studies show that during Li ion migration two kinds of stable LiO<sub>6</sub> units of LATP (upper inset in Figure 1b) exist at the potential energy surface: M1 site located in the LiO<sub>6</sub> octahedrons and M2 site located at each bend of the conduction channels. The migration mode of Li ions in LATP is cooperative; that is, two Li ions at adjacent M1 and M2 sites migrate in pairs which lowers the energy barrier compared to single Li ion migration. 30-33 In detail, along the potential energy surface, Li ions at high-energy sites (M2 sites) migrate downhill; meanwhile, Li ions at low-energy sites (M1 sites) migrate uphill, in which part of the energy barrier is canceled out. These results mean that M1 and M2 sites construct the energy profile, as shown in the lower inset of Figure 1b. A small energy difference between M1 and M2 in site energy corresponds to a flat energy profile and thus favors Li ion migration.

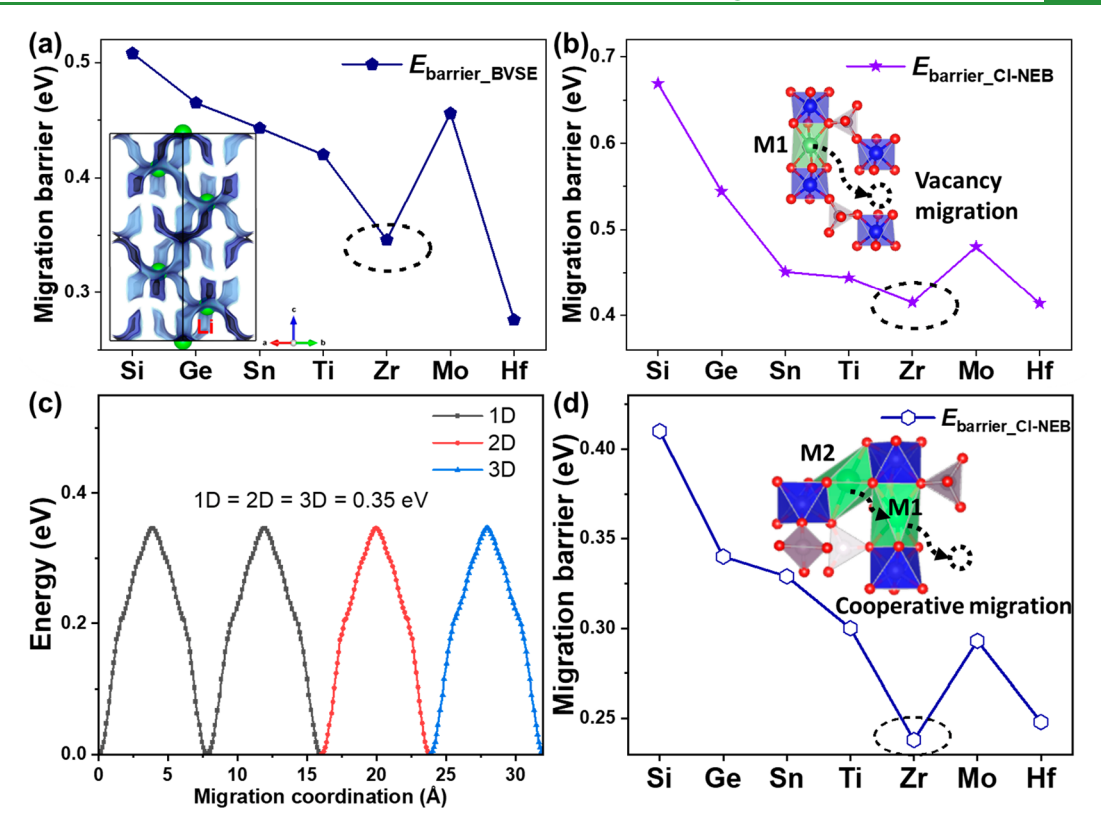


Figure 2. (a, b) Migration barriers calculated from BVSE and Cl-NEB methods along the Li migration channel, respectively. The inset in (a) shows the Li ion diffusion pathway in LXP. The green spheres represent Li ions. Different colors of diffusion pathways correspond to different values of bond valence mismatch, from the highest in black to the lowest in cyan. The inset in (b) shows local configurations along the Li ion migration channel. The red, blue, and green polyhedrons represent O, X, and Li atoms, respectively. The similar variation trend in Figures 2 and 3 reflects the strong correlation between  $XO_6$  units and Li ion conductivity in LXP. (c) Calculated energy potential surface along migration path in LZP via the BVSE method. (d) Calculated migration barriers for the Li ions' cooperative migration in LXP. The green and blue polyhedrons represent  $LiO_6$  and  $XO_6$  units, respectively.

Bearing in mind that M1 and M2 site energy would determine the energy barrier of Li ions' cooperative migration, it is therefore interesting to investigate the effect of XO6 units on relative energies of these two sites in LXP structural motifs. In Figure 1c, we map the site energy profiles to find which LXP structure is the most promising Li ion conductor. Here, the zero value refers to the structure when all Li ions are at M1 sites. The positive value refers to the structure where one Li ion is at a M2 site while the others remain at the M1 site. As shown in Figure 1c, the increasing order of the site energy difference in LXP is Hf < Zr < Mo  $\approx$  Sn  $\approx$  Ti < Ge < Si. It should be noted that LZP and LiHf<sub>2</sub>(PO<sub>4</sub>)<sub>3</sub> (LHP) have a smaller energy difference between M1 and M2 sites, suggesting a much flatter energy profile for Li ion migration and a lower migration barrier. Therefore, we suggest LZP and LHP have lower migration barriers for Li ion migration.

To identify the above suggestion, we then calculate the Li ion migration barriers of LXP with different  $\mathrm{XO}_6$  units within the framework by the BVSE  $^{34,35}$  and the Cl-NEB methods. Figure 2a,b show the migration energy barriers of the Li ion calculated from BVSE and Cl-NEB (vacancy migration) within LXP. An example of a Li ion migration energy profile within LZP by the method of BVSE is shown in Figure 2c. It is not surprising to note that similar trends in migration energy barrier for LXP have been found by BVSE and Cl-NEB methods (Figure 2a,b) as the energy barrier of LZP is the second lowest in the series and the energy barrier of LSiP is the highest. For cooperative migration involving the concerted

knock-off motion of interstitial (M2 site) and lattice Li (M1 site) along the diffusion channel, the calculated energy barriers of the Li ions' cooperative migration by the Cl-NEB method are shown in Figure 2d. The migration barriers of cooperative migration follow the same trend as the migration barriers in Figure 2a,b, with the LZP always having the lowest migration barrier and the LSiP having the highest migration barrier. More importantly, the DFT calculated results of migration barrier have the same changing tendency as the results of site-energy (see Figure 1c), which also testify the correlation between Li migration energy-barrier and Li site-energy tuned by XO<sub>6</sub> units within LXP family.

It is natural to ask what causes the XO6 structural units' sensitivity for the Li ion migration energy barrier. To this end, structural parameters including the bond distances (d(X-O))of  $XO_6$  units (Figure 3a) and  $LiO_6$  units (d(Li-O)) (Figure 3b), the O-O distances (d(O-O)) correlating with bottleneck size for Li ion diffusion (Figure 3c), and the volumes  $(V(PO_4))$  of the PO<sub>4</sub> tetrahedron (Figure 3d) in LXP are first summarized. Of significance to note is that there is the same variation trend of d(X-O), d(Li-O), d(O-O), and  $V(PO_A)$ in LXP. It is important to note that XO6 units initiate the above changing trend, and Figure 3a presents a zigzag manner with XO<sub>6</sub>. The Shannon radii (Å) of the X<sup>4+</sup> ion in octahedra are as follows: Si, 0.40; Ge, 0.53; Sn, 0.69; Ti, 0.61; Zr, 0.72; Mo, 0.65; and Hf, 0.71. The increase of X<sup>4+</sup> ion radius agrees well with the zigzag manner of X-O in Figure 3a. Along the lines in Figures 3a-d, larger cations (Zr4+ and Hf4+) increase

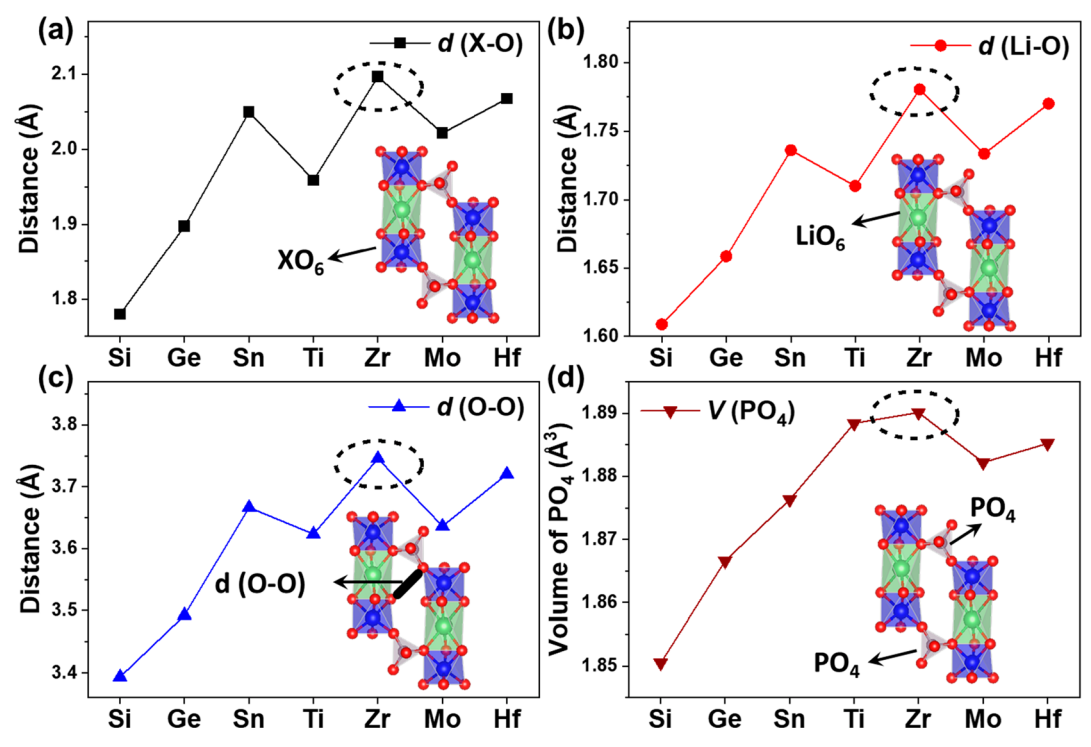


Figure 3. (a) X–O distances in  $XO_6$  units, (b) Li–O distances in  $LiO_6$  units, (c) and O–O distances related to the bottleneck of Li ion migration channel and the volume of  $PO_4$  tetrahedron in LXP. (d) Vacancy migration barrier between two M1 sites in as a function of  $XO_6$  units in LXP. The insets show local configurations of the Li ion migration channel. The green and blue polyhedrons represent  $LiO_6$  and  $XO_6$  units, respectively. The red, blue, and green spheres represent  $O_6$ ,  $O_6$ , and  $O_6$  units, respectively.

the size of lattice volume and widen the diffusion channel of the Li ion. Although the volume changes of PO<sub>4</sub> tetrahedron with XO<sub>6</sub> units in LXP are very small, LiZr<sub>2</sub>(PO<sub>4</sub>)<sub>3</sub> is the one with the largest volume of PO<sub>4</sub> tetrahedron. Because of the octahedra units (LiO<sub>6</sub>-XO<sub>6</sub>) coordinating tetrahedra units (PO<sub>4</sub>) through oxygen bridges to build a stable structural skeleton, the increasing bond distance of Li-O and O-O in LXP will therefore increase the size of the Li diffusion channel. Again, the variation trend in Figure 3 is also consistent with the ordering observed from the site energy in Figure 1c. The above results suggest that the lattice volume with different X<sup>4+</sup> ions in the LXP structure is correlated to the increased Li ion conductivity and reduced activation energy. This point is consistent with the lattice volume design principle in previous studies;<sup>36</sup> that is, increasing the lattice volume can reduce the energy barrier and increase the Li ion conductivity. The site energy approach in Figure 1c, the BVSE method in Figure 2a, the Cl-NEB method in Figure 2b,d, and the lattice volume principle in Figure 3b,c are in broad agreement on the trend of the seven compounds.

In addition to the structural effects on the Li ion migration barrier, the influence of the electronic structure of XO<sub>6</sub> units surrounding the Li ions must be considered. Thus, we carry out crystal orbital Hamilton population (COHP) analysis for all LXP, which is a product of the density of states (DOS) and the overlap Hamiltonian element, an improvement over the classic crystal orbital overlap population.<sup>37,38</sup> With COHP, the chemistry of bonding—antibonding interactions energy regions can be revealed from the solids. Figure 4a—g plot the COHP of the X—O bond as a function of energy in the bulk LXP. Except for the Mo—O bond, all other X—O bonds are indeed strong bonding interactions as COHP is high intensity negative below Fermi level; somewhat unexpectedly, there are also a few

antibonding interactions in the occupied region below the Fermi level, indicating an electronic instability. But for Zr–O, few antibonding interactions are present in LZP for the occupied states. For Mo-O, the Fermi level is located in the region of antibonding states, indicating an inherent instable nature of the structure. Furthermore, a comparison of the ICOHP at the Fermi level (integrated COHP of X-O bonds in LXP) is applied (Figure 4h) to analyze the covalent interaction between X and O. On the basis of the ICOHP value of X-O bonds in LXP, it can be found that the ICOHP value of Zr-O bonds (2.15 eV) is smaller than those of Si-O, Ge-O, and Sn-O bonds (3.20, 2.77, and 2.31 eV, respectively) while is larger than that of Ti-O (1.89 eV), indicating that the covalent effect of LZP is weaker than those of L(Si/Ge/Sn)P but stronger than that of LTP. We evaluate the Li-O bonding by calculating the Li binding energy (i.e., creating one Li vacancy in LXP) as shown in Figure 4i. We find that Li-O bond in LZP is also weaker than those of L(Si/Ge/ Sn)P. In a word, COHP and Li binding energy reveal that the large ZrO<sub>6</sub> and LiO<sub>6</sub> in LZP make the Zr and Li ions loosely bonded to the surroundings as the origins of the covalent character of the two bonds are different. The weaker the X–O bonds, the less negative the O charge; consequently, this results in less electrostatic interaction between Li ions and the oxygen sublattice, leading to lower Li ion migration barriers.

This bonding interaction of X—O can also be understood based on PDOS calculations. The PDOS of X-p or X-d states and O-p orbitals in LXP (Figure 5a) first indicates that the main contribution to the valence band stems from oxygen p-states, while empty p- or d-states of the X atoms contribute mainly to the conduction bands. The magnitude of the LXP gap (except LMoP) is very large (between 2.4 and 7.5 eV), up to the semiconductor, and larger than current sulfide SSEs.

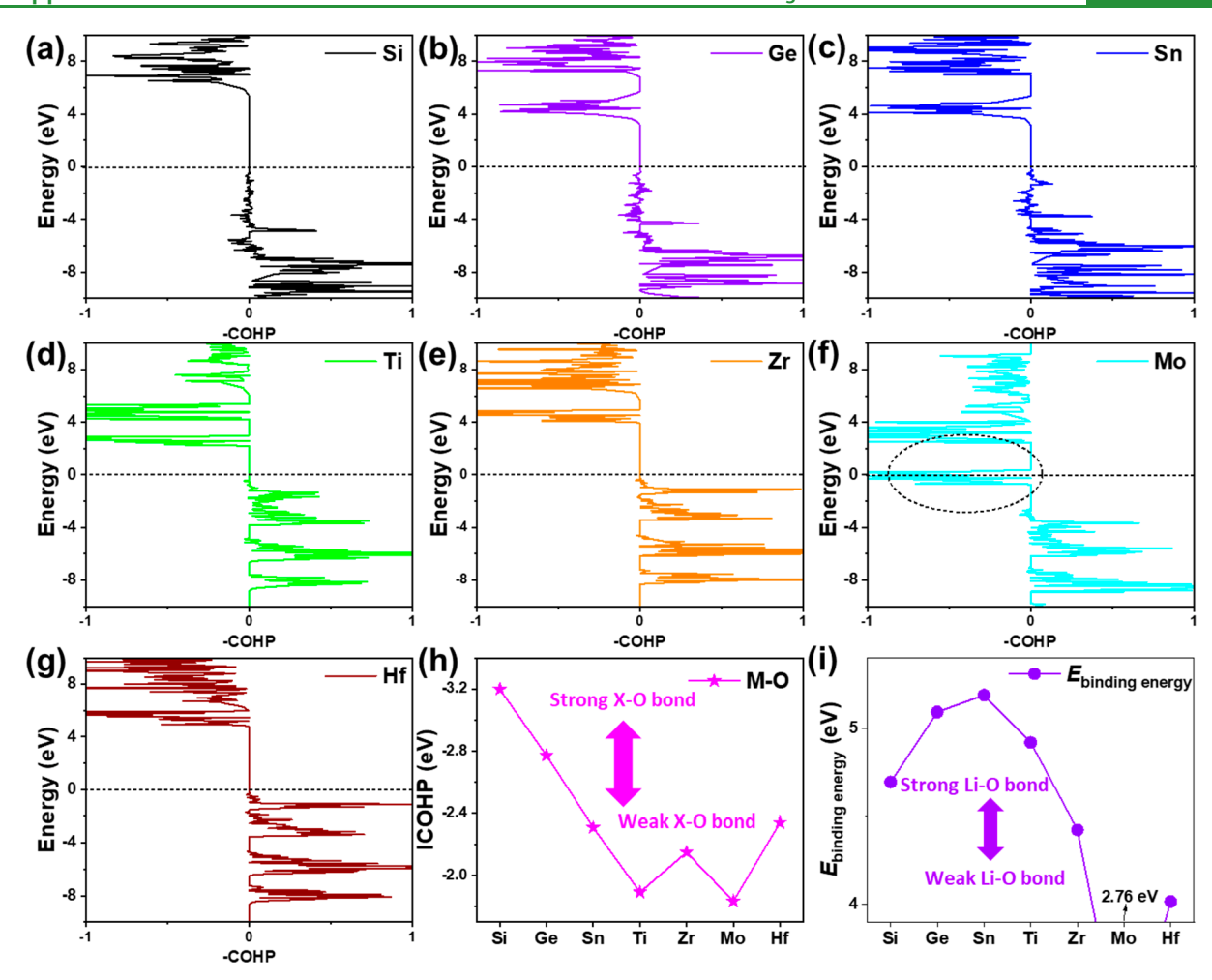


Figure 4. (a-g) Energy states of X–O bonding interaction against COHP in LXP. Values are negative for antibonding and positive for bonding interactions. The horizontal dashed line shows the Fermi level. (h) Integrated COHP (eV) of X–O bonds with different  $X^{4+}$  ions in LXP. (i) Binding energy of Li with different X<sup>4+</sup> ions in LXP.

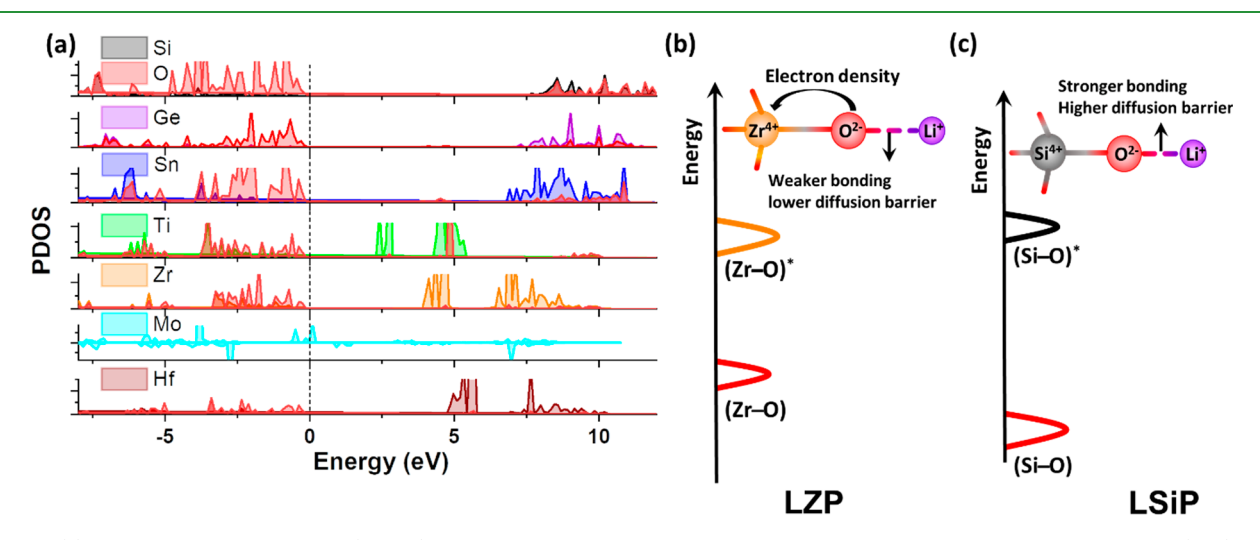


Figure 5. (a) Projected density of states (PDOS) of Si-p, Ge-p, Sn-p, Ti-d, Zr-d, Mo-d, and Hf-d states and O-p states in LXP. (b, c) Sketch showing the changing Coulombic interactions between oxygen and lithium resulting from (Zr-O)\* and (Si-O)\* antibonding states. In LZP, the Zr-O antibonding states accept more excessive negative charges from oxygen because of lower energy levels, weakening the Li-O bonding and reducing Li ion hopping barrier.

The Li ion, in its migration through the oxygen framework, performs bonds with oxygen on which there is a negative charge. The negative charge is an unpaired electron on oxygen on the XO<sub>6</sub> units. Thus, Li migrates in the structure by making bonds with oxygen, and the lone electron pair on oxygen carries excessive negative charge acting as traps for Li<sup>+</sup> ion and

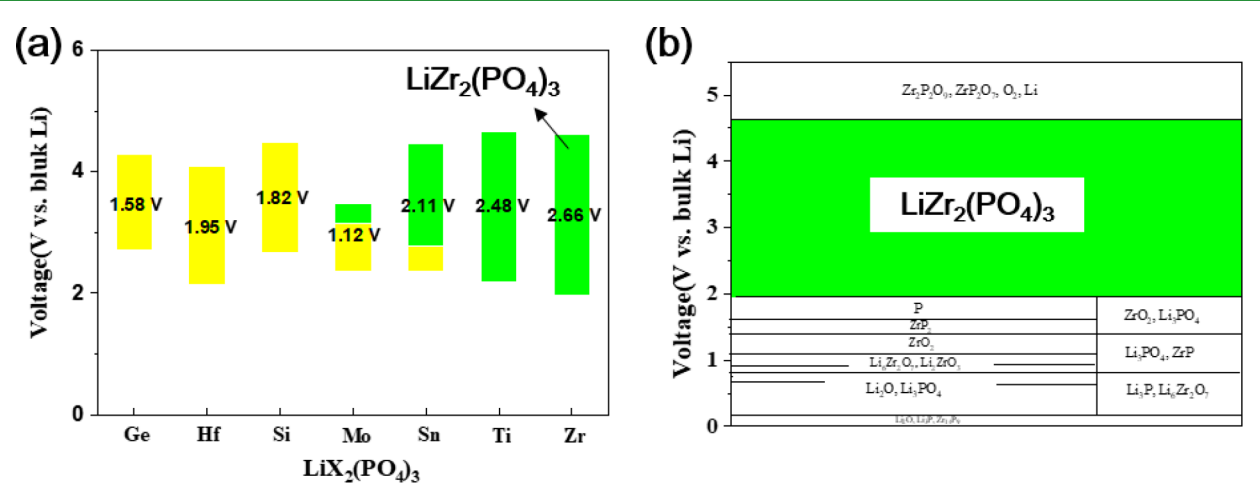


Figure 6. (a) Electrochemical stability window (green bar) for LXP is shown. The yellow region reflects the possible extension of the anodic voltage window as described in the figure. (b) Voltage profile and phase equilibria (anodic and cathodic reactions) of LZP.

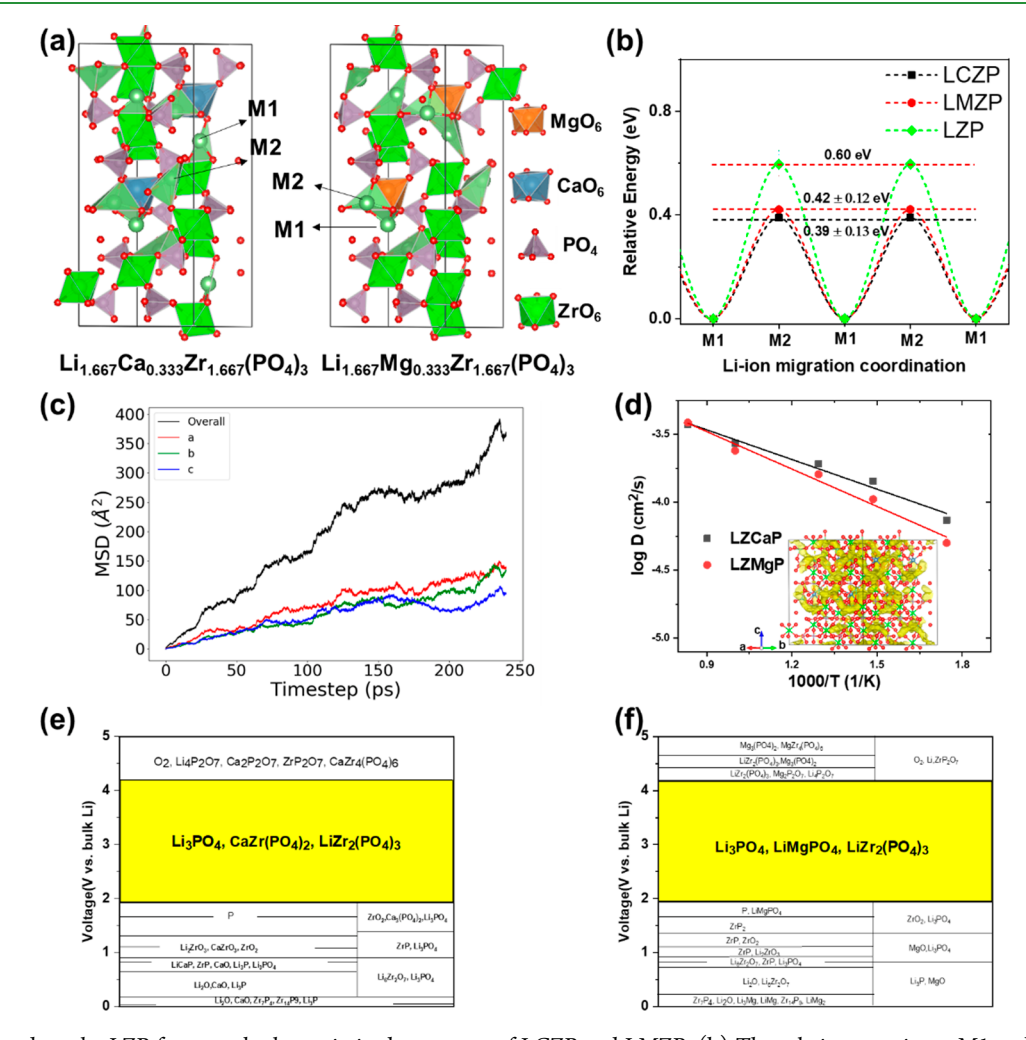


Figure 7. (a) Based on the LZP framework, the optimized structures of LCZP and LMZP. (b) The relative energies at M1 and M2 sites along Li ion migration channels within LCZP, LMZP, and LZP structures. (c) Mean-square displacements (MSD) of Li ions along with three different crystallographic directions as well as the overall value obtained from the AIMD trajectory at 850 K within LCZP. (d) Li diffusivity (D) at various temperatures (T) is fitted linearly for LCZP and LMZP. The inset is the Li ion probability densities (obtained from AIMD simulations at 850 K) in LCZP shown by yellow isosurfaces (plotted at the mean value of the density for each structure). (e, f) Voltage profile and phase equilibria of LCZP and LMZP. PO<sub>4</sub>: pink; ZrO<sub>6</sub>: green; CaO<sub>6</sub>: blue; MgO<sub>6</sub>: orange.

increasing their hopping barriers. This point is important because it means that in LZP the lowered (Zr-O)\* antibonding states would accept excessive negative charges

from oxygen, weakening the Li-O bonding and reducing Li ion migration barrier (Figure 5b). Conversely, in LSiP, the high energy level (Si-O)\* antibonding states may not accept

excessive negative charges from oxygen, leading to a higher Li ion migration barrier (Figure 5c). On the other work, this effect reduces the electrostatic interaction between Li ions and the oxygen framework, leading to a lower Li ion migration. Overall, we suggest that the  $XO_6$  unit sensitivity of Li conductivity can be correlated to the geometrical size of the Li diffusion channel, the site-energy difference of Li, the strength of X–O bonding interaction, and the acceptor energy level of the electron (the position of the antibonding state) within LXP.

To understand the phase stability with respect to a range of possible decomposed systems including elemental, binary, and ternary, we use the GCLP in conjunction with DFT and explore the phase diagram of the Li–X–P–O compound. In the Li<sub>2</sub>O–XO<sub>2</sub>–P<sub>2</sub>O<sub>5</sub> phase diagram, we find the energy above the hull of LSiP, LGP, LSnP, LTP, LZP, LMoP, and LHP with respect to Li<sub>2</sub>O–XO<sub>2</sub>–P<sub>2</sub>O<sub>5</sub> is 0.33, 0.30, 0.25, 0.26, 0.19, 0.25, and 0.17 eV/atom, respectively. We note that the extent of energy above the hull for LTP (0.26 eV/atom) is even larger than that for LZP. For their formation energy, LGP, LSnP, LTP, LZP, and LMoP have negative values with respect to Li<sub>2</sub>O–XO<sub>2</sub>–P<sub>2</sub>O<sub>5</sub> and with –0.19, –0.22, –0.25, –0.29, and –0.24 eV/atom, respectively, indicating they are thermodynamically stable and are less problematic in a battery setup.

For electrochemical stability, after examining the lithiation and delithiation that determine the anodic and cathodic reactions, we evaluate the electrochemical stability of LXP and the phase equilibria of LZP, as shown in Figure 6a,b, respectively. The voltage profile and phase equilibria of other LXP are shown in Figures S1-S6. It is noted that LZP exhibits the widest electrochemical stability window (2.66 V) among LXP. The anodic and cathodic limits of LZP are 1.96 and 4.62 V versus bulk Li, respectively. While LiSi<sub>2</sub>(PO<sub>4</sub>)<sub>3</sub> (LSiP) operates within a narrow stability window (1.82 V, yellowshaded regions) where the LSiP is decomposed into other compounds (LiPO<sub>3</sub>, Li<sub>4</sub>P<sub>2</sub>O<sub>7</sub>, and Ge<sub>5</sub>P<sub>6</sub>O<sub>25</sub>) that are Li ion conducting but electron insulating. The SEI-like (SEI, solid electrolyte interphase) interphases can prevent the further decomposition of LXP and widen the range of the electrochemical stability window. The same situation happens on other LXP (yellow-shaded regions in Figure 6a), such as  $LiGe_{2}(PO_{4})_{3}(LGP)$ , LHP,  $LiMo_{2}(PO_{4})_{3}$  (LMoP), and LiSn<sub>2</sub>(PO<sub>4</sub>)<sub>3</sub> (LSnP). On the other hand, the LZP achieves the lowest reduction potential of as low as 1.96 V compared to 2.19, 2.35, and 2.71 V as found for LTP, LSnP, and LGP, respectively. The phase equilibria of LZP (Figure 6b) suggest that at the Li-metal anode all compounds (Li<sub>2</sub>O, Li<sub>3</sub>P, Li<sub>3</sub>PO<sub>4</sub>, and Li<sub>6</sub>Zr<sub>2</sub>O<sub>7</sub>) but Zr<sub>14</sub>P<sub>9</sub> are SEI-like phases. Indeed, the layer of Li<sub>2</sub>O and Li<sub>3</sub>P has been proven to facilitate the Li passivation at the Li-metal anode.<sup>39</sup> Nevertheless, the practical electrochemical stability of LZP at the Li-metal anode will take further experiments to prove. Considering the ionic conductivity and electrochemical stability together, we suggest LZP is the promising candidate in LXP for SSEs.

**3.2. Further Enhancing Conductivity of LZP by Ca/**  $MgO_6$  Units Substitution. To improve the Li ion conductivity of LZP, we further tune  $ZrO_6$  units by  $CaO_6$  units within the LZP framework. Herein, we consider a low Ca-doping concentration in LZP, and the optimized configurations of  $Li_{1.667}Ca_{0.333}Zr_{1.667}(PO_4)_3$  (LCZP) and  $Li_{1.667}Mg_{0.333}Zr_{1.667}(PO_4)_3$  (LMZP) are shown in Figure 7a. For charge compensation, additional Li atoms are introduced into the M2 sites since there are plenty of M2 sites in LXP

(M2 outnumber M1 sites by more than 3 to 1). We note that Ca/Mg doping changes the Li coordination environment. Li ions within LCZP and LMZP are not at typical octahedral sites, and the LiOx polyhedrons are highly distorted, which may be beneficial to Li ion diffusion. The site energy differences between M1 and M2 in LCZP and LMZP (Figure 7b) are  $0.39 \pm 0.13$  and  $0.42 \pm 0.12$  eV, which is much less than that of LZP (0.60 eV). Thus, (Ca/Mg)O<sub>6</sub> units further smooth the site energy profile of LZP by distorted octahedral sites for Li to occupy. The Li ion diffusivity within the LCZP framework is determined from the AIMD Li ion trajectory of 230 ps, which reveals a nearly isotropic three-dimensional (3D) Li diffusion pattern (Figure 7c). The biggest impact is the improved overall Li diffusivity within the LCZP and LMZP framework with the migration barrier of 0.19 and 0.23 eV, respectively (Figure 7d). Consequently, ionic conductivity for LCZP (~25 mS cm<sup>-1</sup>) and LMZP (~19 mS cm<sup>-1</sup>) at room temperature is as high as ~20 mS cm<sup>-1</sup>. The high Li ion conductivity of LCZP and LMZP comes from the Li excess in the migration channel and the highly distorted LiO<sub>x</sub> polyhedrons.

After examining the whole window, we determine the stability window for LCZP and LMZP in Figure 7e,f. The operating stability window of LCZP and LMZP is up to 2.3 V. We note that SEI-like compounds are formed by the decomposition of LCZP and LMZP compounds when the Li chemical potential approaching the value of 1.9 V. The Liconducting and electronically insulating compounds are electrochemically stable at the range of Li chemical potential. Therefore, self-decomposition compounds (yellow-shaded regions) can provide a passivation layer on the SSEs' surface, which inhibits further electrolyte decomposition and affords the long calendar life required for SSE applications.

## 4. CONCLUSION

In summary, LZP and related LCZP or LMZP compounds are promising materials for SSEs in ASSLBs. We have investigated the influence of XO<sub>6</sub> units in LXP on the Li ion conduction by the concept of cooperative migration, structural features, Li ion vacancy migration, and the electronic structure. Using the BVSE and Cl-NEB methods, we prove that LZP exhibits a smoother energy profile for Li ion migration with a lower energy barrier. The site energy approach, BVSE, and Cl-NEB methods have a similar trend of energy barriers in seven LXP compounds. We attribute the low energy barrier of Li to the large size of the diffusion channel, weak interaction of the Zr-O bond, and easy transfer of excessive electrons from O to Zr; they all weaken the Li-O bonding and reduce the Li migration barrier. The CaO<sub>6</sub> and MgO<sub>6</sub> units greatly improve the ionic conductivity of LZP, which results in the reduced migration barrier as well as offers no regular octahedral site for Li to occupy. In addition, the LZP, LCZP, and LMZP also exhibit a wide electrochemical stability window. This study for the first time shows that ZrO<sub>6</sub>-based LZP fast Li ion conductors can outperform all the other LXP and Ca/Mg doping, further enhancing Li ion conductivity. Such a tuning effect in LXP would provide insight into how Li ion conductivity and stability properties depend on the XO<sub>6</sub> units in the framework, which helps to search for new SSEs with high ionic conductivity and desirable stability.

## ASSOCIATED CONTENT

## Supporting Information

The Supporting Information is available free of charge at https://pubs.acs.org/doi/10.1021/acsami.1c14658.

AIMD simulation details; voltage profile and phase equilibria of LXP (LGP, LTP, LSnP, LSiP, LMoP, and LHP) upon lithiation and delithiation (PDF)

#### AUTHOR INFORMATION

#### **Corresponding Authors**

Bingkai Zhang - Guangzhou Key Laboratory of Clean Transportation Energy Chemistry, School of Chemical Engineering and Light Industry, Guangdong University of Technology, Guangzhou 510006, China; Email: zhangbk@ gdut.edu.cn

Zhan Lin - Guangzhou Key Laboratory of Clean Transportation Energy Chemistry, School of Chemical Engineering and Light Industry, Guangdong University of Technology, Guangzhou 510006, China; Email: zhanlin@ gdut.edu.cn

Feng Pan - School of Advanced Materials, Peking University Shenzhen Graduate School, Shenzhen 518055, China; orcid.org/0000-0002-8216-1339; Email: panfeng@ pkusz.edu.cn

## **Authors**

Zhiwei He - Guangzhou Key Laboratory of Clean Transportation Energy Chemistry, School of Chemical Engineering and Light Industry, Guangdong University of Technology, Guangzhou 510006, China

Jiajie Zhong - Guangzhou Key Laboratory of Clean Transportation Energy Chemistry, School of Chemical Engineering and Light Industry, Guangdong University of Technology, Guangzhou 510006, China

Complete contact information is available at: https://pubs.acs.org/10.1021/acsami.1c14658

### Notes

The authors declare no competing financial interest.

## ACKNOWLEDGMENTS

This work was supported by Guangdong Basic and Applied Basic Research Foundation (2020A1515110046). We thank the Center of Campus Network & Modern Educational Technology, Guangdong University of Technology, Guangdong, China, for providing computational resources and technical support for this work.

## REFERENCES

- (1) Wang, C.; Liang, J.; Zhao, Y.; Zheng, M.; Li, X.; Sun, X. All-Solid-State Lithium Batteries Enabled by Sulfide Electrolytes: From Fundamental Research to Practical Engineering Design. Energy Environ. Sci. 2021, 14 (5), 2577-2619.
- (2) Ye, L.; Li, X. A Dynamic Stability Design Strategy for Lithium Metal Solid State Batteries. Nature 2021, 593 (7858), 218-222.
- (3) Xiao, Y.; Turcheniuk, K.; Narla, A.; Song, A.-Y.; Ren, X.; Magasinski, A.; Jain, A.; Huang, S.; Lee, H.; Yushin, G. Electrolyte Melt Infiltration for Scalable Manufacturing of Inorganic All-Solid-State Lithium-Ion Batteries. Nat. Mater. 2021, 20 (7), 984-990.
- (4) Schwietert, T. K.; Arszelewska, V. A.; Wang, C.; Yu, C.; Vasileiadis, A.; de Klerk, N. J. J.; Hageman, J.; Hupfer, T.; Kerkamm, I.; Xu, Y.; van der Maas, E.; Kelder, E. M.; Ganapathy, S.; Wagemaker, M. Clarifying TheRelationship Between Redox Activity and Electro-

- chemical Stability in Solid Electrolytes. Nat. Mater. 2020, 19 (4),
- (5) Amores, M.; El-Shinawi, H.; McClelland, I.; Yeandel, S. R.; Baker, P. J.; Smith, R. I.; Playford, H. Y.; Goddard, P.; Corr, S. A.; Cussen, E. J. Li<sub>1.5</sub>La<sub>1.5</sub>MO<sub>6</sub> (M = W<sup>6+</sup>, Te<sup>6+</sup>) As ANew Series of Lithium-Rich Double Perovskites for All-Solid-State Lithium-Ion Batteries. Nat. Commun. 2020, 11 (1), 6392.
- (6) Zhang, B.; Zhong, J.; Zhang, Y.; Yang, L.; Yang, J.; Li, S.; Wang, L.-W.; Pan, F.; Lin, Z. Discovering A New Class of Fluoride Solid-Electrolyte Materials Via Screening TheStructural Property of Li-Ion Sublattice. Nano Energy 2021, 79, 105407.
- (7) Chen, R.; Yao, C.; Yang, Q.; Pan, H.; Yu, X.; Zhang, K.; Li, H. Enhancing The Thermal Stability of NASICON Solid Electrolyte Pellets Against Metallic Lithium By Defect Modification. ACS Appl. Mater. Interfaces 2021, 13 (16), 18743-18749.
- (8) Kahlaoui, R.; Arbi, K.; Sobrados, I.; Jimenez, R.; Sanz, J.; Ternane, R. Cation Miscibility and Lithium Mobility in NASICON  $\text{Li}_{1+x}\text{Ti}_{2-x}\text{Sc}_x(\text{PO}_4)_3 \ (0 \le x \le 0.5)$  Series: A Combined NMR and Impedance Study. Inorg. Chem. 2017, 56 (3), 1216-1224.
- (9) Maldonado-Manso, P.; Losilla, E. R.; Martínez-Lara, M.; Aranda, M. A. G.; Bruque, S.; Mouahid, F. E.; Zahir, M. High Lithium Ionic Conductivity in The Li<sub>1+x</sub>Al<sub>x</sub>Ge<sub>y</sub>Ti<sub>2-x-y</sub>(PO<sub>4</sub>)<sub>3</sub> NASICON Series. Chem. Mater. 2003, 15 (9), 1879-1885.
- (10) Abramchuk, M.; Voskanyan, A. A.; Arinicheva, Y.; Lilova, K.; Subramani, T.; Ma, Q.; Dashjav, E.; Finsterbusch, M.; Navrotsky, A. Energetic Stability and Its Role in The Mechanism of Ionic Transport in NASICON-Type Solid-State Electrolyte Li<sub>1+x</sub>Al<sub>x</sub>Ti<sub>2-x</sub>(PO<sub>4</sub>)<sub>3</sub>. J. Phys. Chem. Lett. 2021, 12 (18), 4400-4406.
- (11) Arbi, K.; Hoelzel, M.; Kuhn, A.; García-Alvarado, F.; Sanz, J. Structural Factors That Enhance Lithium Mobility in Fast-Ion  $\text{Li}_{1+x}\text{Ti}_{2-x}\text{Alx}(\text{PO}_4)_3$  (0  $\leq x \leq 0.4$ ) Conductors Investigated By Neutron Diffraction in The Temperature Range 100-500 K. Inorg. Chem. 2013, 52 (16), 9290-9296.
- (12) Xiao, W.; Wang, J.; Fan, L.; Zhang, J.; Li, X. Recent Advances in Li<sub>1+x</sub>Al<sub>x</sub>Ti<sub>2-x</sub>(PO<sub>4</sub>)<sub>3</sub>Solid-State Electrolyte for Safe Lithium Batteries. Energy Stor. Mater. 2019, 19, 379-400.
- (13) Xiao, Y.; Wang, Y.; Bo, S.-H.; Kim, J. C.; Miara, L. J.; Ceder, G. Understanding Interface Stability in Solid-State Batteries. Nat. Rev. Mater. 2020, 5, 105-126.
- (14) Lang, B.; Ziebarth, B.; Elsässer, C. Lithium Ion Conduction in LiTi<sub>2</sub>(PO<sub>4</sub>)<sub>3</sub> and Related Compounds Based on The NASICON Structure: A First-Principles Study. Chem. Mater. 2015, 27 (14), 5040-5048.
- (15) Zhang, B.; Lin, Z.; Dong, H.; Wang, L.-W.; Pan, F. Revealing Cooperative Li-Ion Migration in Li<sub>1+x</sub>Al<sub>x</sub>Ti<sub>2-x</sub>(PO<sub>4</sub>)<sub>3</sub>Solid State Electrolytes with High Al Doping. J. Mater. Chem. A 2020, 8 (1), 342 - 348.
- (16) El-Shinawi, H.; Regoutz, A.; Payne, D. J.; Cussen, E. J.; Corr, S. A. NASICON  $LiM_2(PO_4)_3$ Electrolyte (M = Zr) and Electrode (M = Ti) Materials for All Solid-State Li-Ion Batteries with High Total Conductivity and Low Interfacial Resistance. J. Mater. Chem. A 2018, 6 (13), 5296-5303.
- (17) Kresse, G.; Furthmüller, J. Efficiency of Ab-initio Total Energy Calculations for Metals and Semiconductors Using aPlane-Wave Basis Set. Comput. Mater. Sci. 1996, 6 (1), 15-50.
- (18) Blöchl, P. E. Projector Augmented-Wave Method. Phys. Rev. B: Condens. Matter Mater. Phys. 1994, 50 (24), 17953-17979.
- (19) Kresse, G.; Furthmüller, J. Efficient Iterative Schemes for Ab Initio Total-Energy Calculations Using APlane-Wave Basis Set. Phys. Rev. B: Condens. Matter Mater. Phys. 1996, 54 (16), 11169-11186.
- (20) Perdew, J. P.; Chevary, J. A.; Vosko, S. H.; Jackson, K. A.; Pederson, M. R.; Singh, D. J.; Fiolhais, C. Atoms, Molecules, Solids, and Surfaces: Applications of The Generalized Gradient Approximation for Exchange and Correlation. Phys. Rev. B: Condens. Matter Mater. Phys. 1992, 46 (11), 6671-6687.
- (21) Henkelman, G.; Uberuaga, B. P.; Jónsson, H. A Climbing Image Nudged Elastic Band Method for Finding Saddle Points and Minimum Energy Paths. J. Chem. Phys. 2000, 113 (22), 9901-9904.

- (22) Kresse, G.; Furthmüller, J. Efficient Iterative Schemes for Ab Initio Total-Energy Calculations Using APlane-Wave Basis Set. *Phys. Rev. B: Condens. Matter Mater. Phys.* **1996**, 54 (16), 11169–11186.
- (23) Kirklin, S.; Meredig, B.; Wolverton, C. High-Throughput Computational Screening of New Li-Ion Battery Anode Materials. *Adv. Energy Mater.* **2013**, 3 (2), 252–262.
- (24) Wolverton, C.; Siegel, D. J.; Akbarzadeh, A.; Ozoliņš, V. Discovery of Novel Hydrogen Storage Materials: An Atomic Scale Computational Approach. *J. Phys.: Condens. Matter* **2008**, 20 (6), 064228.
- (25) Richards, W. D.; Miara, L. J.; Wang, Y.; Kim, J. C.; Ceder, G. Interface Stability in Solid-State Batteries. *Chem. Mater.* **2016**, 28 (1), 266–273.
- (26) Ong, S. P.; Wang, L.; Kang, B.; Ceder, G. Li-Fe-P-O<sub>2</sub> Phase Diagram From First Principles Calculations. *Chem. Mater.* **2008**, *20* (5), 1798–1807.
- (27) Ong, S. P.; Mo, Y.; Richards, W. D.; Miara, L.; Lee, H. S.; Ceder, G. Phase Stability, Electrochemical Stability and Ionic Conductivity of The  $\text{Li}_{10\pm 1}\text{MP}_2\text{X}_{12}$  (M = Ge, Si, Sn, Al or P, and X = O, S or Se) Family of Superionic Conductors. *Energy Environ. Sci.* **2013**, *6* (1), 148–156.
- (28) Ong, S. P.; Richards, W. D.; Jain, A.; Hautier, G.; Kocher, M.; Cholia, S.; Gunter, D.; Chevrier, V. L.; Persson, K. A.; Ceder, G. Python Materials Genomics (Pymatgen): A Bobust, Open-Source Python Library for Materials Analysis. *Comput. Mater. Sci.* 2013, 68, 314–319
- (29) Banerjee, S.; Zhang, X.; Wang, L.-W. Motif-Based Design of An Oxysulfide Class of Lithium Superionic Conductors: Toward Improved Stability and Record-High Li-Ion Conductivity. *Chem. Mater.* **2019**, *31* (18), 7265–7276.
- (30) He, X.; Zhu, Y.; Mo, Y. Origin of Fast Ion Diffusion in Super-Ionic Conductors. *Nat. Commun.* **2017**, 8 (1), 15893.
- (31) Zhang, Z.; Zou, Z.; Kaup, K.; Xiao, R.; Shi, S.; Avdeev, M.; Hu, Y.-S.; Wang, D.; He, B.; Li, H.; Huang, X.; Nazar, L. F.; Chen, L. Correlated Migration Invokes Higher Na<sup>+</sup>-Ion Conductivity in NASICON-Type Solid Electrolytes. *Adv. Energy Mater.* **2019**, 9 (42), 1902373.
- (32) Zhang, B.; Weng, M.; Lin, Z.; Feng, Y.; Yang, L.; Wang, L.-W.; Pan, F. Li-ion Cooperative Migration and Oxy-sulfide Synergistic Effect in Li<sub>14</sub>P<sub>2</sub>Ge<sub>2</sub>S<sub>16-x</sub>O<sub>x</sub>Solid-State-Electrolyte Enables Extraordinary Conductivity and High Stability. *Small* **2020**, *16*, 1906374.
- (33) Zhang, B.; Yang, L.; Wang, L.-W.; Pan, F. Cooperative Transport Enabling Fast Li-ion Diffusion in Thio-LISICON Li<sub>10</sub>SiP<sub>2</sub>S<sub>12</sub>Solid Electrolyte. *Nano Energy* **2019**, *62*, 844–852.
- (34) Chen, H.; Wong, L. L.; Adams, S. SoftBV-a Software Tool for Screening the Materials Genome of Inorganic Fast Ion Conductors. *Acta Crystallogr., Sect. B: Struct. Sci., Cryst. Eng. Mater.* **2019**, 75 (1), 18–32
- (35) Wong, L. L.; Phuah, K. C.; Dai, R.; Chen, H.; Chew, W. S.; Adams, S. Bond Valence Pathway Analyzer-An Automatic Rapid Screening Tool for Fast Ion Conductors within softBV. *Chem. Mater.* **2021**, 33 (2), 625–641.
- (36) Bachman, J. C.; Muy, S.; Grimaud, A.; Chang, H.-H.; Pour, N.; Lux, S. F.; Paschos, O.; Maglia, F.; Lupart, S.; Lamp, P.; Giordano, L.; Shao-Horn, Y. Inorganic Solid-State Electrolytes for Lithium Batteries: Mechanisms and Properties Governing Ion Conduction. *Chem. Rev.* **2016**, *116* (1), 140–162.
- (37) Dronskowski, R.; Bloechl, P. E. Crystal Orbital Hamilton Populations (COHP): Energy-Resolved Visualization of Chemical Bonding in Solids Based on Density-Functional Calculations. *J. Phys. Chem.* **1993**, 97 (33), 8617–8624.
- (38) Deringer, V. L.; Tchougréeff, A. L.; Dronskowski, R. Crystal Orbital Hamilton Population (COHP) Analysis As Projected from Plane-Wave Basis Sets. *J. Phys. Chem. A* **2011**, *115* (21), 5461–5466. (39) Nazri, G. Preparation, Structure and Ionic Conductivity of Lithium Phosphide. *Solid State Ionics* **1989**, 34 (1–2), 97–102.